Nanoscale

Monovalent Sulfur Oxoanions Enable Millimeter-Long Single Crystalline *h*-WO_3 Nanowire Synthesis

Journal:	*Nanoscale*
Manuscript ID	NR-ART-12-2019-010565.R2
Article Type:	Paper
Date Submitted by the Author:	23-Mar-2020
Complete List of Authors:	Zhang, Guozhu ; Kyushu University, Wang, Chen; Kyushu University Mizukami, Wataru; Kyushu University Hosomi, Takuro; Kyushu University Nagashima, Kazuki; Kyushu University, Yoshida, Hideto; Osaka University, The Institute of Scientific and Industrial Research Nakamura, Kentaro; Kyushu University Takahashi, Tsunaki; Kyushu University Kanai, Masaki; Kyushu University Yasui, Takao; Nagoya University, Department of Applied Chemistry Aoki, Yuriko; Kyushu University, Faculty of Engineering Sciences, Department of Material Sciences Baba, Yoshinobu; Nagoya University, Yanagida, Takeshi; Kyushu Sangyo Daigaku,

ARTICLE

Monovalent Sulfur Oxoanions Enable Millimeter-Long Single Crystalline *h*-WO_3 Nanowire Synthesis

Received 00th January 20xx,
Accepted 00th January 20xx

DOI: 10.1039/x0xx00000x

Guozhu Zhang,[a] Chen Wang,[a] Wataru Mizukami,[b] Takuro Hosomi,[a] Kazuki Nagashima,[a] Hideto Yoshida,[c] Kentaro Nakamura,[a] Tsunaki Takahashi,[a] Masaki Kanai,[a] Takao Yasui,[d] Yuriko Aoki,[b] Yoshinobu Baba[d] and Takeshi Yanagida[a,b]*

Here we discuss a chemical capping misunderstanding, which has intrinsically hindered to extend the length of hexagonal(*h*)-WO_3 nanowires in previous studies. Although divalent sulfate ions (SO_4^{2-}) have been strongly believed as efficient capping ions to direct an anisotropic *h*-WO_3 nanowire growth, we found that the presence of SO_4^{2-} is highly detrimental for the anisotropic crystal growth of *h*-WO_3 nanowires, and a monovalent sulfur oxoanion (HSO_4^-) rather than the SO_4^{2-} only substantially promotes the anisotropic *h*-WO_3 nanowire growths. *Ab initio* electronic structure simulations reveal that the monovalent sulfur oxoanions are more preferentially able to cap the sidewall plane (100) of *h*-WO_3 nanowires due to the lower hydration energy when compared with SO_4^{2-}. Based on this capping strategy, using monovalent sulfur oxoanion ($CH_3SO_3^-$), which cannot generate divalent sulfur oxoanions, we successfully fabricate ultra-long *h*-WO_3 nanowires up to millimeter range (1.2 mm) for the wider range of precursor concentrations. We demonstrate the feasibility of these millimeter-long *h*-WO_3 nanowires for electrical sensing of molecules (lung cancer biomarker: nonanal) on the flexible substrates, which can be operated at room temperature with the mechanical flexibility even bending cycles up to 10^4 times due to the enhanced textile effect.

Introduction

Understanding a selectivity of crystal growth direction using capping molecules is important to spatially design inorganic/organic nanomaterials for various applications including catalysts[1-5], sensors[6-10] and energy devices[11-16]. The chemical capping method usually utilizes structure directing agents, which preferentially cap a specific crystal face to obtain the selectivity of crystal growth direction.[17-24] Since such chemical capping occurs during a dynamic crystal growth process at relatively harsh conditions, it is frequently difficult to obtain the exact physical pictures of capping behaviors.[25-27] For example, hexagonal tungsten oxide (*h*-WO_3) nanowires are often hydrothermally synthesized by introducing a capping molecule. As the structure-directing agents, sulfate salts, such as Na_2SO_4, K_2SO_4 and $(NH_4)_2SO_4$, are typically employed.[28-37] During the crystal growth process, SO_4^{2-} has been suggested as an efficient capping molecule, which preferentially caps the sidewall plane (100) of *h*-WO_3 nanowires. [30-31] Indeed, the addition of these sulfate salts remarkably increases the aspect ratio of WO_3 nanowire up to 625.[35] However, further increase of SO_4^{2-} concentration frequently results in not only nanowire forms but also the other complex nanostructures including bamboo-like[36] and even triggers a transformation of crystal phase to pyrochlore-phase microcrystals from hexagonal-phase nanowires.[37] The addition of sulfate ions during WO_3 nanowire growth must cause more complex molecular phenomena, which cannot be explained by existing SO_4^{2-} capping model.[30-31]

Here, we argue a long-standing misunderstanding of traditional SO_4^{2-} based chemical capping models for *h*-WO_3 hydrothermal nanowire synthesis. We experimentally and theoretically reveal that the presence of SO_4^{2-} is detrimental for *h*-WO_3 hydrothermal nanowire growth, and the monovalent sulfur oxoanion (HSO_4^-) rather than SO_4^{2-} only substantially promotes the anisotropic *h*-WO_3 nanowire growth. By precisely controlling the amount of monovalent sulfur oxoanions during crystal growth, we successfully fabricate ultra-long WO_3 nanowires up to 1.2 mm range. In addition, we demonstrate the applicability of these millimeter-long *h*-WO_3 nanowires for electrical sensing of molecules (biomarker in breath: nonanal) on the flexible substrates. The millimeter-long WO_3 nanowires exhibit the superior mechanical flexibility and durability due to the enhanced textile effect.

Results and discussion

First, we show the effects of both a capping molecule source Na_2SO_4 concentration (C_{NS}) and a tungsten precursor

[a] Institute for Materials Chemistry and Engineering, Kyushu University, 6-1 Kasuga-Koen, Kasuga, Fukuoka, 816-8580, Japan.
[b] Interdisciplinary Graduate School of Engineering Sciences, Kyushu University, 6-1 Kasuga-Koen, Kasuga, Fukuoka, 816-8580, Japan.
[c] The Institute of Scientific and Industrial Research, Osaka University, 8-1 Mihogaoka, Ibaraki, Osaka 567-0047 Japan.
[d] Graduate School of Engineering, Nagoya University, Furo-cho, Chikusa-ku, Nagoya 464-8603, Japan
†Electronic Supplementary Information (ESI) available: [details of any supplementary information available should be included here]. See DOI: 10.1039/x0xx00000x

(polytungstic acid) concentration (C_W) on WO_3 nanowire growths. The C_{NS} was controlled from 0mM to 50 mM, and C_W was ranged from 0.1 mM to 54.4 mM (the growth results that without capping agent (C_{NS}, 0mM) are shown in Supporting Information, Fig. S1). Fig. 1a shows the variation map of fabricated nanostructures as a function of both concentrations, respectively. Detailed SEM images are shown in Supporting Information, Fig. S2 and Fig. S3. Here, oxalic acid ($H_2C_2O_4$) is utilized to guarantee that sufficient amount of tungsten precursor colloidal particles can be generated in solution for subsequent hydrothermal growth (Figure S4).[30] The other experimental details can be seen in Method section. The concentration mapping data can be classified into three regions named "R1" to "R3". Each includes (R1) no visible crystals when C_W is below 1 mM, (R2) nanowires and nanorods structures with hexagonal WO_3 crystal structures, or (R3) microplate structures with pyrochlore WO_3 crystal phase. The typical capping agent (Na_2SO_4) concentration dependent SEM and XRD data are shown in Fig. 1b and 1c (TEM characterizations of the as-grown nanowires are shown in Supporting Information Fig. S5). First type transition is from R1 to R2 (Type 1) which appears when C_W increases. Such transition is no longer observable above 10 mM of C_{NS}. The second type transition is from R1 to R3 (Type 2) emerges when increasing C_W with higher C_{NS}. The third type transition is from R2 to R3 (Type 3), which is observed above ~1 mM of C_w when increasing C_{NS}. According to the WO_3 nanostructure growth results in Fig. 1a, the *h*-WO_3 nanowire growth rate mapping data is plotted in Fig. 1d. Interestingly, we found that long *h*-WO_3 can only be formed near the boundary regions of these three regions. And significantly long WO_3 nanowires, whose lengths are up to 500 μm with the diameter of 100 nm (Supporting Information Fig. S6), are obtained within this boundary. Thus, the control of both C_{NS} and C_W critically determines the emergence of fabricated nanostructure forms, crystal phases (hexagonal or pyrochlore phases), and the fabrication of long WO_3 nanowires. More importantly, traditional SO_4^{2-} based chemical capping models seem to be not appropriate to explain these experimental trends. Based on previously proposed model for WO_3 nanowire formation mechanism, SO_4^{2-} must play an important role as a capping molecule for the sidewall of nanowires.[30-31] However, the trend of Fig. 1 when increasing C_{NS} as a capping molecule source is not consistent with this traditional SO_4^{2-} capping model.[30-31] This is because the increase of C_{NS} resulted in the transition (Type 3) from nanowire to microplate. Thus, this contradictive result demonstrates the inability of existing conventional model based on only SO_4^{2-} capping for WO_3 anisotropic nanowire crystal growth.

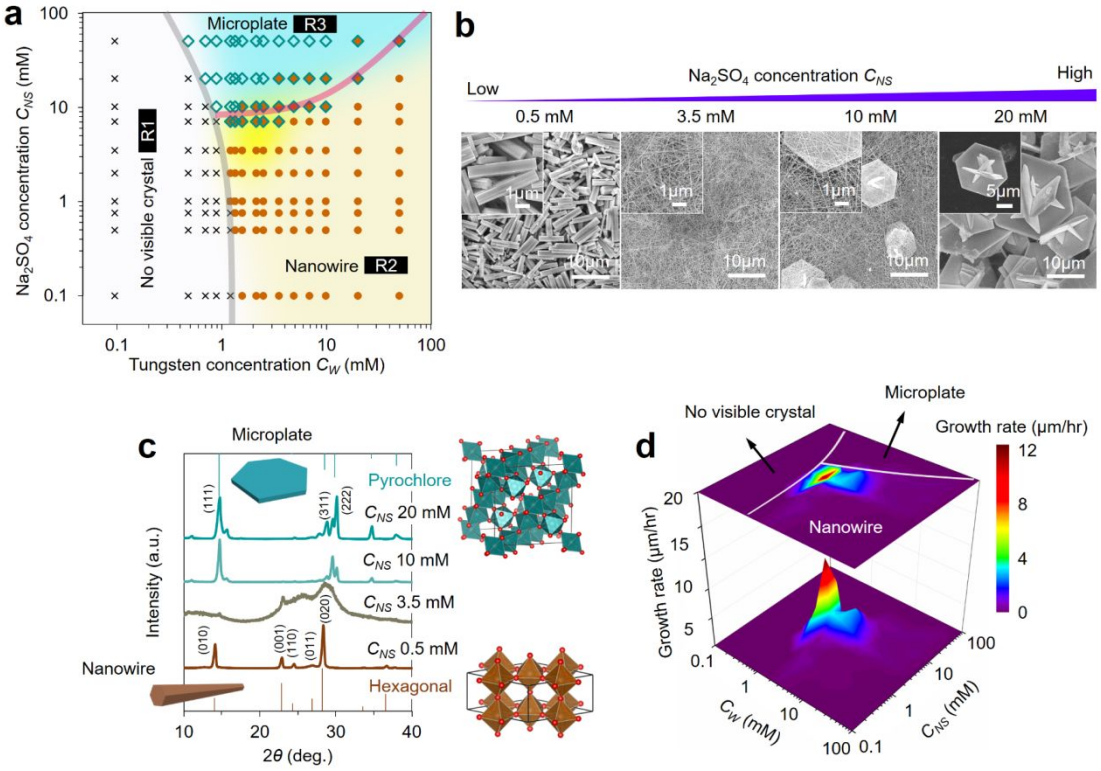

Fig. 1. (a) Variation of morphology and crystal structures (R1: × No visible crystal, R2: ● Nanowire, R3: ◇ Microplate, and ◈ mixture of nanowire and microplate). (b) Typical SEM images of Na_2SO_4 concentration (C_{NS}) dependent WO_3 nanostructures. (c) XRD characterization of the WO_3 nanostructures from (b). (d) *h*-WO_3 nanowire growth rate data.

In order to explain above inconsistency between the experimental trend in Fig. 1 and existing traditional SO_4^{2-} capping model, we consider the presence of HSO_4^-, because HSO_4^- rather than SO_4^{2-} can be the dominant species in a certain condition (e.g. low pH range), $HSO_4^- \leftrightarrow SO_4^{2-} + H^+$, *p*Ka=1.99.[38] Fig. 2b shows the calculated concentrations of two different

charged states of sulfur oxoanions (HSO_4^- and SO_4^{2-}) from Na_2SO_4 when varying C_{NS} with the fixed value (2.72mM) of C_w. The calculations were performed by using a commercial software (Visual MINTEQ) (Supporting Information Fig. S7). For these simulations, the ion concentrations were calculated by using experimentally measured values of pH (Supporting Information Fig. S8) and the temperature for crystal growth experiments. When increasing C_{NS}, SO_4^{2-} tends to be the major species because the increase of C_{NS} results in an increase of pH to promote deprotonation of HSO_4^- (Fig. 2b). On the other hand, HSO_4^- tends to be dominant for the lower C_{NS} concentration range below 20 mM, as also highlighted in the plotted data of the concentration difference data ($\Delta C = C_{HSO_4^-} - C_{SO_4^{2-}}$) between HSO_4^- and SO_4^{2-}. ΔC data exhibits the maximum around 7 mM of C_{NS}. Interestingly, this concentration range is consistent with the appearance of long WO_3 nanowires in Fig. 1. At the higher C_{NS} range where SO_4^{2-} is the dominant sulfur anion, pyrochlore WO_3 microplates emerge in Fig. 1. As such, in comparison with experimental data in Fig. 1, these calculated data of sulfur oxoanions proposes a model that explains the experimentally observed anisotropic WO_3 nanowire growth in terms of the presence of HSO_4^- rather than previously proposed SO_4^{2-} as structure directing capping species. This model is based on the experimental results that long WO_3 nanowires can be formed for HSO_4^- dominated concentration range (*i.e.* $\Delta C>0$). In order to further validate this capping model for the wider range of experiments employed, we calculate the populations of two sulfur oxoanions via measuring pH values for the wide ranges of C_w and C_{NS}. The measured pH values at growth temperature when varying both C_w and C_{NS} are shown in Fig. S5. Increase of C_w results in a decrease of pH value due to the increased concentration of tungstic acid (H_2WO_4). When increasing C_{NS}, the pH value increases because Na_2SO_4 act as a buffer in an acidic solution due to its weak basicity.[39] Based on these pH values, we can calculate the populations of two sulfur oxoanions (Supporting Information Fig. S9). In addition, $\Delta C/C_w$ values are plotted in Fig. 2c, because the capping efficiency of HSO_4^- onto tungsten oxide nuclei is related to $\Delta C/C_w$. As can be seen, the calculated $\Delta C/C_w$ data shows the maximum at concentration range, where long WO_3 nanowires were observed in Fig. 1b. Thus, there is a certain correlation between the presence of HSO_4^- in a solution and the appearance of long WO_3 nanowires.

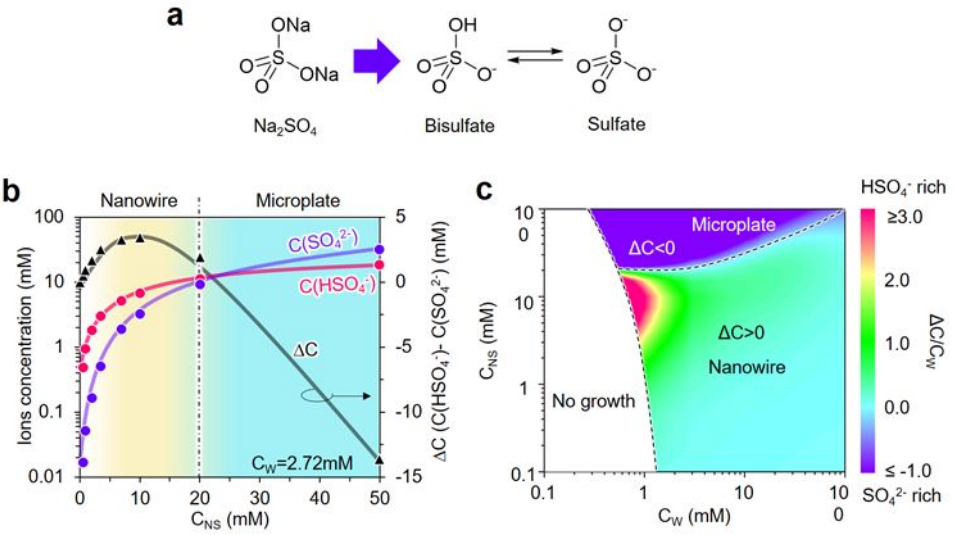

Fig. 2. (a) Schematic illustration of ionization for Na_2SO_4 in a solution. (b) Calculated concentrations of two different charged states of sulfur oxoanions (HSO_4^- and SO_4^{2-}) from Na_2SO_4 when varying C_{NS}. (c) Calculated $\Delta C/C_w$ data when varying C_w and C_{NS}.

Above results infer that HSO_4^- rather than SO_4^{2-} should be able to more preferentially cap a sidewall of *h*-WO_3 (100) nanowires, enhancing the anisotropic nanowire crystal growth. To further validate this model, we intentionally change the equilibrium concentration of HSO_4^- by reducing the growth solution pH from 1.68 to 1.12 with 1M NaOH. The total amount of Na_2SO_4 was controlled to be 20 mM. As speculated, the equilibrium ion concentration of HSO_4^- increases with decreasing the pH value via a protonation (Supporting Information Fig. S10). Although the pH variation range is relatively narrow-1.12-1.68, the effect is significant on the fabricated WO_3 nanostructure morphology (Supporting Information Fig. S11). At pH value of 1.68, microplate morphology with pyrochlore WO_3 crystal phase (Supporting Information Fig. S12) is only observable. While decreasing pH value strongly enhances the anisotropic hexagonal WO_3 nanowire growth (Supporting Information Fig. S12). Thus, these series of results further experimentally support a model based on HSO_4^- rather than previously suggested SO_4^{2-} as efficient capping species for an anisotropic WO_3 nanowire crystal growth.

To obtain a microscopic understanding as to the selective capping behaviours of HSO_4^- or SO_4^{2-} onto WO_3 nanostructures surfaces, we perform *ab initio*-density functional theory (DFT) simulations. In gas phase condition, the binding energy of a single HSO_4^- or SO_4^{2-} onto the WO_3 crystal plane can be

estimated by considering the difference of total energies of the combined and the isolated systems with the following formula- $E_{Binding} = E_{HSO_4^-/SO_4^{2-}+WO_3} - (E_{HSO_4^-/SO_4^{2-}} + E_{WO_3})$. However, in the aqueous solution, HSO_4^- or SO_4^{2-} strongly hydrates with the surrounding water molecules.[40-41] Therefore, the calculations must consider such hydration effects to compare the capping effect of HSO_4^- or SO_4^{2-} onto the WO_3 surfaces. As illustrated in Fig. 3a, a competition between an ion adsorption and a hydration determines whether the capping effect of molecules onto solid surfaces within an aqueous solution occurs. Consequently, the net binding energy of capping molecules (HSO_4^- or SO_4^{2-}) may be formulated as $\Delta E_{Net\_binding} = E_{binding} - \alpha E_{Hydration}$. $\alpha E_{Hydration}$ is the hydration energy loss after the molecules binding on the WO_3 surface (α, hydration energy loss ratio[42]). The net binding energy (Δ*E*) of capping molecules (HSO_4^- or SO_4^{2-}) on hexagonal WO_3 nanowire top (001) and sidewall (100) planes are calculated by the method described in the Method Section and Supporting Information. Fig. 3b shows the calculated the net biding energy of both capping molecules (HSO_4^- and SO_4^{2-}) onto the sidewall (100) plane of *h*-WO_3 (calculation data of (001) plane is shown in Supporting Information, Fig. S17). As can be seen, the net biding energy for HSO_4^- on (100) plane is negative, whereas SO_4^{2-} exhibits the positive net binding energy due to the higher stability of hydration (Table 1). In addition, the net binding energies of both HSO_4^- and SO_4^{2-} on (100) plane are positive, indicating that they are unable to adsorb on (100) plane in the water phase. As a result, the nanowire sidewall (100) planes are hindered for further growth, while the growth of top (001) planes are selectively facilitated. These results are also consistent with previous data, in which a hydration energy of SO_4^{2-} (-1080.2kJ/mol)[43] is reported to be four times higher than that of HSO_4^- (-285.1kJ/mol)[42]. These simulations also infer that in addition to the hydration effects, less Coulomb repulsion effect of monovalent sulfur oxoanion than divalent sulfate ion might increase the adsorbed ion surface density, which also promotes a capping effect. Thus, these *ab initio*-DFT simulations highlight that HSO_4^- preferentially adsorbs onto the (100) plane of *h*-WO_3, while SO_4^{2-} is strongly hydrated rather than being onto the (100) plane of *h*-WO_3. This strong hydration effect of SO_4^{2-} is well-known as Hofmeister series.[44-45] In addition, this strong hydration effect can be experimentally confirmed in Fig. 1a, where the critical nucleation concentration decreases with increasing C_{NS} above 5mM of C_{NS} due to the strong hydration effect of SO_4^{2-}. These simulation results give an interpretation for a model based on a HSO_4^- capping mechanism during hexagonal WO_3 nanowire growth trend in Fig. 1.

Table 1. Binding energies, $\Delta E_{binding}$ *and* $\Delta E_{Net\_binding}$, of different capping species on *h*-WO_3 (001) and (100) planes.

Capping species	Binding energy/kJ/mol			
	In vapor phase $\Delta E_{binding}$		In water phase $\Delta E_{Net\_binding}$	
	(001)	(100)	(001)	(100)
SO_4^{2-}	-448.8	-618.4	74.9	60.3
HSO_4^-	-297.7	-315.3	56.1	-64.9

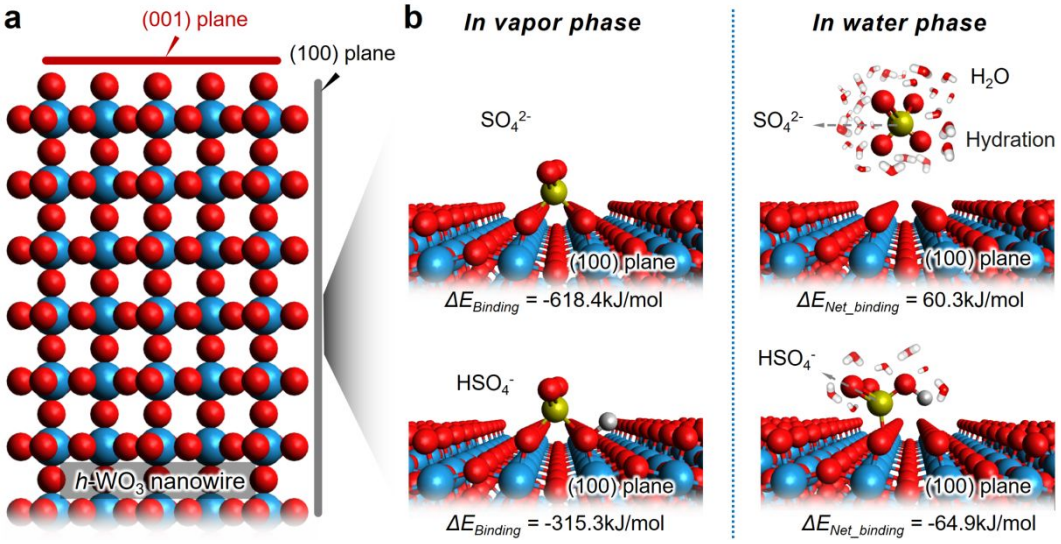

Fig. 3. (a) Crystal structure of hexagonal WO_3. (b) Calculated binding energy of both sulfur oxoanions (HSO_4^- and SO_4^{2-}) on the plane (100) of hexagonal WO_3 in vapour and water phase. The coordination structures are simulated by DFT calculation.

Above experimental and theoretical data consistently highlight that the presence of monovalent HSO_4^- rather than previously proposed divalent SO_4^{2-} essentially promotes an anisotropic WO_3 nanowire growth. This suggests that suppressing the formation of divalent sulfur oxoanions in a solution must be able to solve above detrimental effect due to the presence of SO_4^{2-}. However, the controllability of concentration of HSO_4^- is substantially limited due to the occurrence of protonation or deprotonation in a solution as

long as we employ sulfate salts including Na_2SO_4, K_2SO_4 and $(NH_4)_2SO_4$. To overcome this essential difficulty, we employ sodium mesylate (CH_3SO_3Na) as a capping molecule source instead of Na_2SO_4. It is because the corresponding anion $CH_3SO_3^-$ has a structure in which one of the hydroxyl group on HSO_4^- is replaced by a methyl group,[46] and therefore $CH_3SO_3^-$ does not be dissociated further to a divalent anion (Fig. 4a). Fig. 4b shows the applicability of the present method for the wider concentration range in comparison with Fig. 1b. Interestingly, the effect of CH_3SO_3Na is significant, as can be seen in the SEM images (Fig. 4c). Note that only at the highest concentration of CH_3SO_3Na, WO_3 microplate emerges due to the decomposition of $CH_3SO_3^-$ into SO_4^{2-} at temperature range employed.[47] The long nanowire morphology with the hexagonal phase WO_3 can be maintained even increasing a concentration of CH_3SO_3Na (C_{MS}) up to 50 mM (Supporting Information Fig. S13 and Fig. S14), which is in sharp contrast to the case for $NaSO_4$, where the pyrochlore crystal phase WO_3 microplates emerges in Fig. 1a. Since this method using CH_3SO_3Na does not suffer from the presence of SO_4^{2-} even varying C_{MS}, the controllability of fabricating long WO_3 nanowires is much superior to that of conventional Na_2SO_4 based method. By utilizing CH_3SO_3Na as a capping molecule source, the length of nanowires was reached up to 1.2 mm, as shown in Fig. 4d (High magnification SEM image is shown in Fig. S15). Surprisingly, these ultra-long nanowires can be assembled to centimeter-long nanowire yarn during growth (Fig. 4e and Video S1). Compare with reported WO_3 nanowires that obtained through hydrothermal method, the as-grown nanowires in this work show the highest length and aspect ratio (Supporting Information Table S1, Supporting Information Fig. S16). Thus, the charged state of capping molecules critically determines the degree of anisotropic WO_3 nanowire growth.

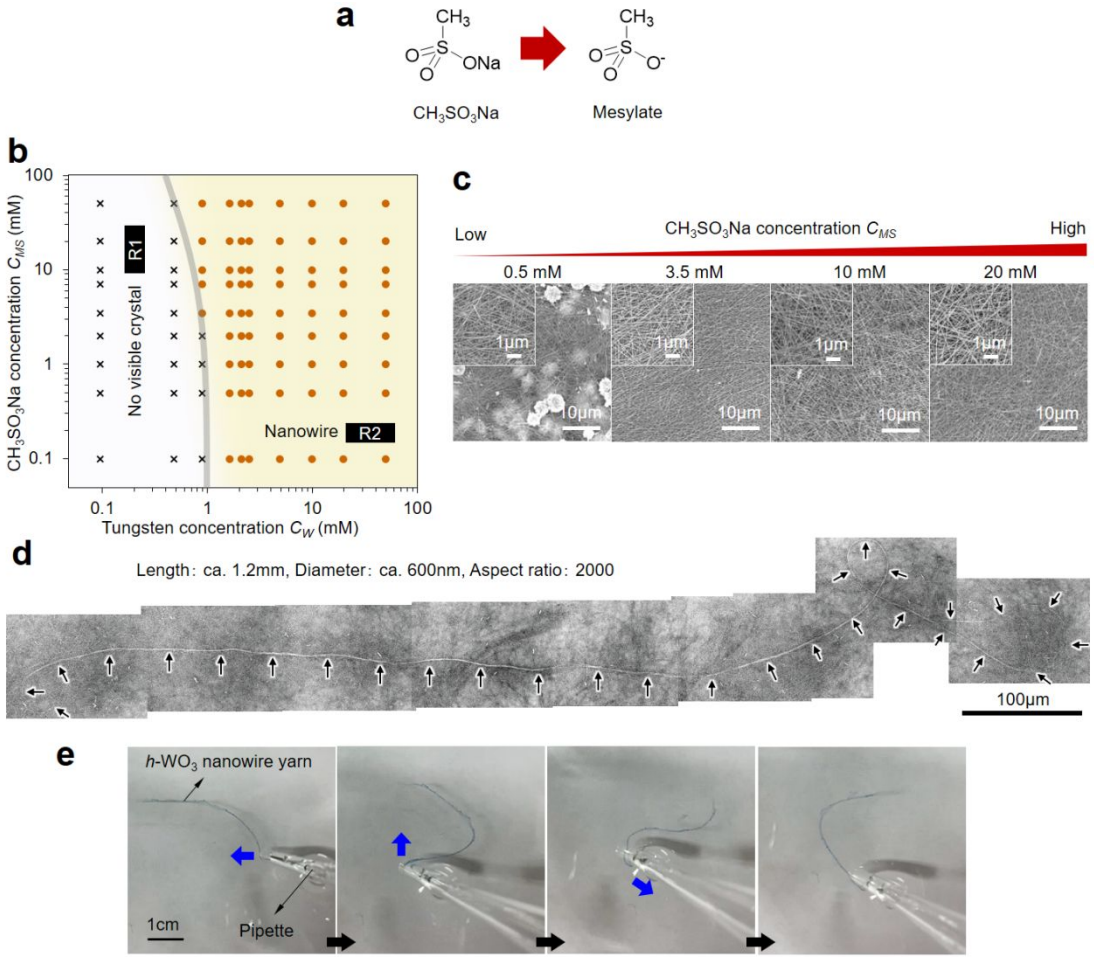

Fig. 4. (a) Schematic illustration of ionization for CH_3SO_3Na in a solution. (b) Effect of CH_3SO_3Na concentration (C_{MS}) on the fabricated WO_3 nanostructure morphology (SEM images). (c) Variation of morphology and crystal structures when varying C_W and C_{MS}, (d) millimeter-long *h*-WO_3 nanowire when controlling C_W (2.18mM) and C_{MS} (6mM). (e) Manipulation of the as-grown *h*-WO_3 nanowire yarn (assembled from ultra-long nanowire).

Finally, we show the applicability of fabricated long hexagonal WO_3 nanowires towards molecule sensing devices with the robust mechanical flexibility. As the model target molecules, we employ a nonanal (as a lung cancer biomarker in breath[48]). Fig. 5a shows photographs of as grown ultra-long hexagonal WO_3 nanowire film and fabricated flexible nanowire film sensors on polyethylene naphthalate (PEN) substrate. The details of fabrication of nanowires and flexible sensor devices including the nanowire transfer process can be seen in Method section. Note that the WO_3 nanowire films strongly sticks onto

the PEN substrate even mechanically bending situations for cycles up to 10^4 times (Supporting Information Fig. S23). Fig. 6b shows typical data of sensing response to 2.67 ppm nonanal (the gas concentration was calibrated by GC-MS, Supporting Information Fig. S18) at room temperature. To study the effect of nanowire length on the flexible sensor characteristics, the two data of relatively long WO_3 nanowires (Aver. ~200 μm, containing millimeter-long nanowire) and relatively short WO_3 nanowires (Aver. ~15 μm) with similar diameters (~100nm) were shown in the figure. Both the two nanowire sensor devices exhibit the sensing response to nonanal molecules, and the long nanowire based sensor presents a greater sensing performance as compared with that of short nanowire. This sensor response can be recovered to the initial state when removing nonanal (Supporting Information Fig. S19 and S20). To our best knowledge, this nonanal electrical sensing operated at room temperature have not been reported so far.[49-50] Since such diameter of WO_3 nanowire cannot be fully depleted at room temperature[51] and there are no metal-semiconductor contact barriers formed in the nanowire sensor device (Fig. S21), the sensing performance is predominately controlled by the nanowire junctions.[52] That is, introducing a nonanal decreases the nanowire junction resistance of sensors. In addition, ultraviolet–visible absorption spectra and Photoluminescence spectra (Fig. S22) providing clear evidences that the long *h*-WO_3 nanowires contain higher density of oxygen vacancy defects as compared with the short nanowire.[53] Thus, a greater nonanal sensing performance is presented in the long nanowire based sensor device before mechanical bending.

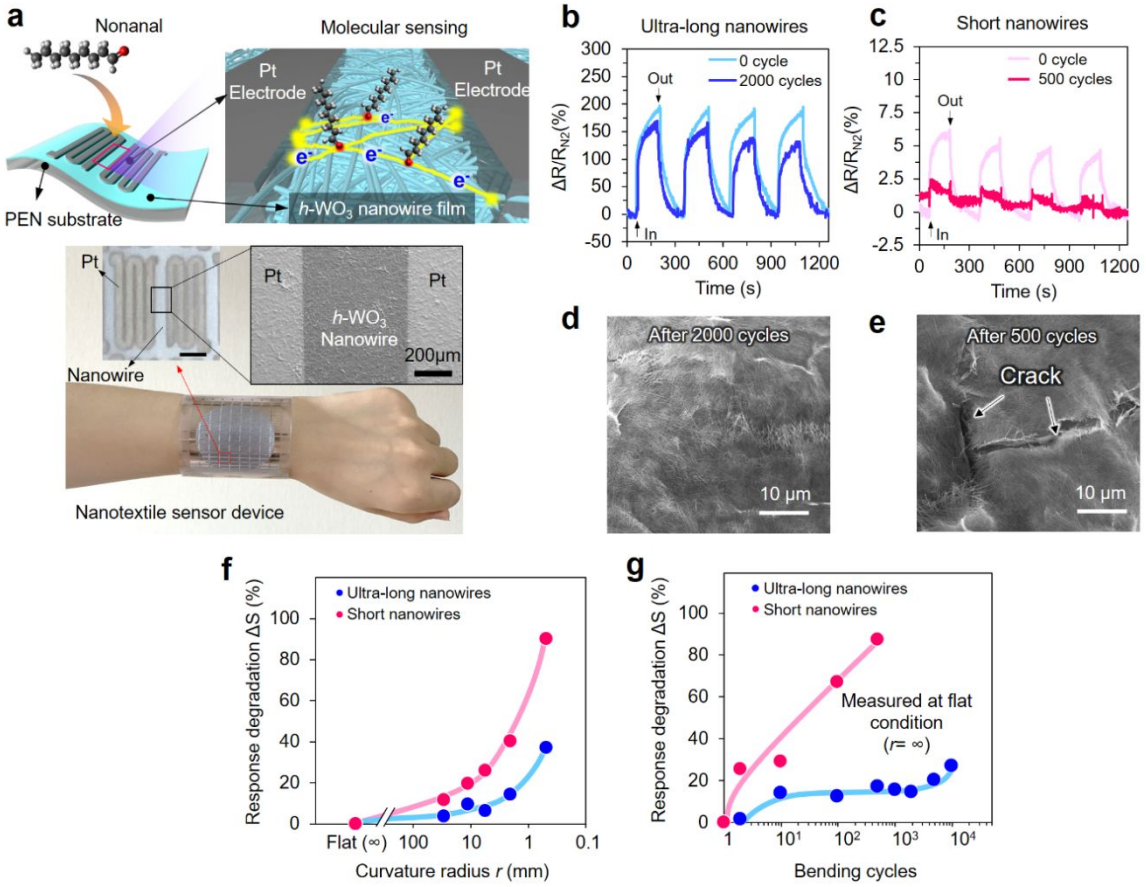

Fig. 5. (a) Schematic illustration of the *h*-WO_3 nanowires based molecular sensor for lung cancer biomarker detection (upper), and structure of as-fabricated nanotextile sensor device (lower) (scale bar 2mm). Response curve of the (b) ultra-long and (c) short *h*-WO_3 nanowire-based sensor to 2.67 ppm of nonanal that tested with and without mechanical bending at room temperature, (d) and (e) images of the long and short *h*-WO_3 nanowire-based sensor after 2000/500 cycles of mechanical bending, (f) response of the ultra-long *h*-WO_3 nanowire-based sensor to 2.67 ppm of nonanal under different bending curvature radii and (g) bending cycles.

As is known, the implementation of micro- or nanoscale structural forms of inorganic semiconductor materials in flexible electronics relies critically on their ability to be bent repeatedly without fracture.[54] Thus here, we mainly focused on the bendability of the nanowire-based sensor device. Fig. 5b and 5c shows that the mechanical bending process strongly inhibits the sensor response only for device composed of relatively short nanowires, but not for that of relatively long nanowires. It was found the long WO_3 nanowire sensor device shows only a slight sensing performance degradation (8.6% of the initial value) after subjecting to 2000 cycles of bending (Fig. 5b), while the short WO_3 nanowire sensor device shows the rapid degradation of sensing performance to a nonanal even after bending for 500 cycles (Fig. 5c). As shown in Fig. 5d and 5e, the film degradation with cracks is responsible to explain this

discrepancy between the two nanowire sensor devices. The mechanical bending process over 500 times results in a crack within nanowire films composed of relatively short nanowires. However, such mechanically induced film cracks are much less observable for sensor device composed of relatively long nanowires. This is solely due to the enhanced textile effect of longer nanowire devices when compared with short nanowires. Specific speaking, due to the intrinsically high-aspect-ratio and spatial entanglement of the long nanowires, the constructed nanowire network can extremely prevent the formation of the cracks when strains are applied, thereby reducing the dependence of the resistance change on the strain.[55] Furthermore, we investigate the effects of the bending strain and the cycle endurance on the sensing performance. Fig. 5f shows the results of bending curvature radius (strain) dependent sensing responses, implying that the sensor performances exhibit slight degradations when the curvature radius lower than 2.1mm. Even for bending with a curvature radius as small as 0.5mm (high bending strain), the sensor still remains good sensing properties (36.9% degradation). While the short nanowire based sensor presents a dramatic performance degradation as the curvature radius lower than 20 mm, and almost lost all the performance with curvature radius of 0.5 mm. In addition, bending cycle endurance data is also shown in Fig. 5g. There are no significant sensing performance degradations for the long WO_3 nanowire based flexible sensor up to 10^4 cycles (Supporting Information Fig. S23). But the short nanowire based sensor shows a poor mechanical bending performance. These results highlight the superior molecule sensing properties with the excellent mechanical flexibility due to the enhanced textile effects of long WO_3 nanowires.

Conclusions

In summary, we firstly found that the monovalent sulfur oxoanions (HSO_4^- and $CH_3SO_3^-$) rather than previously proposed SO_4^{2-} substantially enhances the anisotropic nanowire growth of *h*-WO_3. In fact, the presence of SO_4^{2-} hinders the anisotropic crystal growth of WO_3. *ab initio*-density functional theory (DFT) simulations reveal that the monovalent sulfur oxoanions are more effectively able to cap the sidewall plane (100) of hexagonal WO_3 nanowires due to the lower hydration energy when compared with SO_4^{2-}. Based on this capping strategy using $CH_3SO_3^-$, which can generate only monovalent sulfur oxoanions, we successfully achieve ultra-long of WO_3 nanowires up to millimeter range (1.2 mm). Furthermore, we demonstrate the feasibility of these millimeter-long WO_3 nanowires for electrical sensing of molecules (lung cancer biomarker: nonanal) on the flexible substrates, which can be operated at room temperature with the mechanical flexibility even bending cycles up to 10^4 times due to the enhanced textile effect.

Experimental

Fabrication of WO_3 nanowires

h-WO_3 nanowires were fabricated by two steps which including the polytungstic acid sol synthesis and the nanowires growth. For polytungstic acid sol synthesis, first, 4 g of tungsten powder (W) was dissolved in 30 g of hydrogen peroxide solution (H_2O_2, 30 wt. % in H_2O) with an ice bath under stirring. After the W powder completely dissolved, a transparent solution was obtained. Then, Pt foil was immersed in the solution to catalytically remove the excess H_2O_2. As no bubble generated, the as-synthesized polytungstic acid sol were diluted by the distilled water to 100 g. Afterward, 12.5 g of polytungstic acid sol (2.72 mM W) was transferred to a 100 mL capacity of autoclave and 37.5 g distilled water was added to further diluted the solution. Then, 0.5625 g (6.25 mM) oxalic acid ($H_2C_2O_4$) were added to the mixture and NaOH solution (1 mol/L) was used to adjust the pH of the mixture solution to 1.68. Following, 0.5 g (3.5 mM) of sodium sulfate (Na_2SO_4) was added in the growth solution. After the complete dissolution of Na_2SO_4, sealed the Teflon-lined high-pressure autoclave and transfer to the sintering furnace and maintained at 200 °C for 24 hours. Finally, WO_3 Nanowires were obtained after centrifugation of the products and washed by distilled water to remove the excess ions.

Structural characterizations.

The structural characterizations of grown WO_3 nanowires are performed by using x-ray diffraction (Rigaku, SmartLab, 45kV, 40mA), field emission scanning electron microscopy-SEM (JEOL, JSM-7610F) equipped with energy dispersive X-ray spectroscopy (EDS) and transmission electron microscopy-TEM (JEOL, JEM-ARM200F, 200kV).

Molecule sensing procedure.

The as-grown WO_3 nanowires were firstly washed with diluted water for several times and fished by the polyethylene naphthalate (PEN) substrate. By heating the PEN substrate at 100 °C for 15 min, the residual water can be removed. After the removing of the water, WO_3 nanowires were stuck on PEN substrate and formed as uniform nanowire film. Then, radiofrequency (RF) sputtering technique was used to deposit the platinum (Pt) electrode with a stainless steel mask. To enhance the adhesion between the substrate and the Pt electrodes, a thin layer (~5 nm) of titanium (Ti) was sputtered ahead of the Pt. The sensing performance to nonanal was carried out by a self-made chamber combined with the Keithley 4200A-SCS Parameter Analyzer (TEKTRONIX, INC.) at room temperature. Resistance of the WO_3 nanowire device under N_2 was recorded as baseline (R_{N2}). The resistance upon exposure of nonanal gas (produced by bubbling liquid nonanal solution) was noted as R_{gas}. Sensitivity (S) was defined as $\Delta R/R_{N2}$, $\Delta R=(R_{N2}-R_{gas})$. Sensitivity degradation (ΔS) was defined as $(S_{flat} - S_{bending})/S_{flat}$. All the sensing tests were carried out under a DC bias voltage of 1V. nonanal gas was produced by bubbling liquid nonanal solution with high pure N_2, and its concentration was calibrated by the gas chromatograph mass spectroscopy (GCMS, Shimadzu GCMS-QP2010 Ultra) with temperature control system (GL Sciences, OPTIC-4). The flow rate of dry air and the nonanal gas were controlled at 200sccm during the sensing performance tests.

Ab initio electronic structure simulations.

We used density functional theory (DFT) to compute adsorption energies of SO_4^{2-} and HSO_4^- on the *h*-WO_3 (100) and (001) planes. Different levels of theory were combined via the ONIOM

extrapolation scheme, which allowed both to consider hydration effects and to refine results from pure DFT by exact-exchange hybrid DFT calculations.

Conflicts of interest

There are no conflicts to declare.

Acknowledgements

This work was supported by KAKENHI (No.26706005, No.17H04927, No.15H03528). This work also was supported by Dynamic Alliance for Open Innovation Bridging Human, Environment and Materials in Network Joint Research Center for Materials and Devices. The computation in this work has been done using the facilities of RIIT, Kyushu University, and the Supercomputer Center, the Institute for Solid State Physics, the University of Tokyo. This work was performed under the Cooperative Research Program of "Network Joint Research Center for Materials and Devices" and the MEXT Project of "Integrated Research Consortium on Chemical Sciences"

Notes and references

1 T. Tachikawa, S. Yamashita, T. Majima, *J. Am. Chem. Soc.* 2011, **133**, 7197-7204.
2 M. B. J. Roeffaers, B. F. Sels, H. Uji-i, F. C. De Schryver, P. A. Jacobs, D. E. De Vos, J. Hofkens, *Nature* 2006, **439**, 572.
3 R. Xu, D. S. Wang, J. Y. Zhang, Y. D. Li, *Chem.–Asian J.* 2006, **1**, 888-893.
4 A. Trovarelli, J. Llorca, *ACS Catal.* 2017, 7, 4716-4735.
5 H. Zhang, Jin, M. Xiong, Y. Lim, B. Xia, Y. *Acc. Chem. Res.* 2013, **46**, 1783-1794.
6 S. Tian, F. Yang, D. Zeng, D. Xie, *J. Phys. Chem. C* 2012, **116**, 10586-10591.
7 S. Deng, V. Tjoa, H. Fan, M. Tan, H. R. Sayle, D. C. Olivo, M. Mhaisalkar, S. Wei, J. Sow, C. H. *J. Am. Chem. Soc.* 2012, **134**, 4905-4917.
8 M. D. Arienzo, L. Armelao, A. Cacciamani, C. M. Mari, S. Polizzi, R. Ruffo, R. Scotti, A. Testino, L. Wahba, F. Morazzoni, *Chem. Mater.* 2010, **22**, 4083-4089.
9 X. Han, M. Jin, S. Xie, Q. Kuang, Z. Jiang, Y. Jiang, Z. Xie, L. Zheng, *Angew. Chem., Int. Ed.* 2009, **48**, 9180-9183.
10 M. H. Huang, P.-H. Lin, *Adv. Funct. Mater.* 2012, **22**, 14-24.
11 T. Sheng, Y. Xu, Y. Jiang, L. Huang, N. Tian, Z. Zhou, I. Broadwell, S. Sun, *Acc. Chem. Res.* 2016, **49**, 2569-2577.
12 C. Hu, M. Li, J. Qiu, Y.-P. Sun, *Chem. Soc. Rev.* 2019,*48*, 2315-2337.
13 H. J. Yin, Z. Y. Tang, *Chem. Soc. Rev.* 2016, ***45***, 4873-4891.
14 J. E. ten Elshof, H. Y. Yuan, P. G. Rodriguez, *Adv. Energy Mater.* 2016, **6**, 1600355.
15 H. Zhang, Q. Yun, Q. Lu, X. Zhang, C. Tan, *Angew. Chem., Int. Ed.* 2018, ***57***, 626-646.
16 C.-C. Chiang, C.-Y. Hung, S.-W. Chou, J.-J. Shyue, K.-Y. Cheng, P.-J. Chang, Y.-Y. Yang, C.-Y. Lin, T.-K. Chang, Y. Chi, H.-L. Chou, P.-T. Chou, *Adv. Funct. Mater.* 2018, ***28***, 1703282.
17 Y. Sun, Y. Xia, *Science* 2002, ***298***, 2176-2179.
18 Y. Xia, Y. Xiong, B. Lim, S. E. Skrabalak, *Angew. Chem., Int. Ed.* 2009, **48**, 60-103.
19 J. Zeng, Y. Zheng, M. Rycenga, J. Tao, Z.-Y. Li, Q. Zhang, Y. Zhu, Y. Xia, *J. Am. Chem. Soc.* 2010, **132**, 8552-8553.
20 P. D. Cozzoli, A. Kornowski, H. Weller, *J. Am. Chem. Soc.* 2003, **125**, 14539-14548.
21 S. M. Lee, S. N. Cho, J. Cheon, *Adv. Mater.*2003, ***15***, 441-444.
22 M. Jin, G. He, H. Zhang, J. Zeng, Z. Xie, Y. Xia, *Angew. Chem., Int. Ed.* 2011, **50**, 10560-10564.
23 S. F. Tan, G. Bisht, U. Anand, M. Bosman, X. E. Yong, U. Mirsaidov, *J. Am. Chem. Soc.* 2018, ***140***, 11680-11685.
24 C. G. Garcia Núñez, A. F. Braña, N. López, B. J. García, *Nano Lett.* 2018, ***18***, 3608-3615.
25 Q. Fu, X. Bao, *Chem. Soc. Rev.* 2017, **46**, 1842-1874.
26 P. Liu, R. Qin, G. Fu, N. Zheng, *J. Am. Chem. Soc.* 2017 **139**, 2122-2131.
27 T. H. Yang, Y. Shi, A. Janssen, Y. Xia, *Angew. Chem., Int. Ed.* 2019.
28 X. W. Lou, H. C. Zeng, *Inorg. Chem.* 2003, **42**, 6169-6171.
29 X. L. Li, J. F. Liu, Y. D. Li, *Inorg. Chem.* 2003, **42**, 921-924.
30 Z. Gu, Y. Ma, W. Yang, *Chem. Commun.* 2005, **0**, 3597-3599.
31 Z. Gu, T. Zhai, B. Gao, X. Sheng, Y. Wang, H. Fu, Y. Ma, J. Yao, *J. Phys. Chem. B* 2006, **110**, 23829-23836.
32 Z. Gu, H. Li, T. Zhai, W. Yang, Y. Xia, Y. Ma, J. Yao, *J. Solid State Chem.* 2007, **180**, 98-105.
33 X. C. Song, Y. F. Zheng, E. Yang, Y. Wang, *Mater. Lett.* 2007, **61**, 3904-3908.
34 K. Huang, Q. Pan, F. Yang, S. Ni, X. Wei, D. He, *J. Phys. D-Appl. Phys.* 2008, **41**, 155417.
35 A. Phuruangrat, D. J. Ham, S. J. Hong, S. Thongtem, J. S. Lee, *J. Mater. Chem.* 2010, **20**, 1683-1690.
36 J. Zhang, J. P. Tu, X. H. Xia, X. L. Wang, C. D. Gu, *J. Mater. Chem.* 2011, **21**, 5492-5498.
37 J. Shi, G. Hu, R. Cong, H. Bu, N. Dai, *New J. Chem.* 2013, **37**, 1538-1544.
38 D. H. Ripin, Evans p*K*a table. 2005.
39 L. Lerner, CRC Press, 2011.
40 R. Caminiti, G. Paschina, G. Pinna, M. Magini, Chem. *Phys. Lett.* 1979, **64**, 391-395.
41 T. I. Yacovitch, T. Wende, L. Jiang, N. Heine, G. Meijer, *J. Phys. Chem. Lett.* 2011, **2**, 2135-2140.
42 Y. Marcus, J. Chem. Soc., Faraday Trans. 1987, **83**, 339-349.
43 J. O. Bockris, M. Gamboa-Aldeco, M. Szklarczyk, *J. Electroanal. Chem.* 1992, **339**, 355-400.
44 Y. Zhang, P. S. Cremer, *Annu. Rev. Phys. Chem.* 2010, **61**, 63-83.
45 S. Nihonyanagi, S. Yamaguchi, T. Tahara, *J. Am. Chem. Soc.* 2014, **136**, 6155-6158.
46 C. H. Wei, B. E. Hingerty, *Acta Cryst.* 1981, **37**, 1992-1994.
47 P. C. Hu, M. E. Tuvell, *J. Am. Oil Chem.' Soc.* 1988, **65**, 1007-1012.
48 P. Fuchs, C. Loeseken, J. K. Schubert, W. Miekisch, *Int. J. Cancer* 2010, **126**, 2663-2670.
49 T. Itoh, T. Nakashima, T. Akamatsu, N. Izu, W. Shin, *Sens Actuators B: Chem. 2013*, **187**, 135-141.
50 Y. Masuda, T. Itoh, W. Shin, K. Kato, *Sci. Rep.* 2015, **5**, 10122.
51 A. Labidi, C. Lambert-Mauriat, C. Jacolin, M. Bendahan, M. Maaref, K. Aguir, *Sens Actuators B: Chem*. 2006, **119**, 374-379.
52 A. Rothschild, Y. Komem, *J. Appl. Phys.* 2004, **95**, 6374-6380.
53 S. Cong, Y. Yuan, Z. Chen, J. Hou, M. Yang, Y. Su, Y. Zhang, L. Li, Q. Li, F. Geng, Z. Zhao, *Nat. Commun.*, 2015, **6**, 7800.
54 A. J. Baca, J. H. Ahn, Y. Sun, M. A. Meitl, E. Menard, H. S. Kim, W. M. Choi, D. H. Kim, Y. Huang, J. A. Rogers, *Angew. Chem. Int. Ed.* 2008, **47**, 5524-5542.
55 S. Gong, W. Cheng, *Adv. Electron. Mater.* 2017, **3**, 1600314.

A table of contents entry

Monovalent sulfur oxoanions (HSO_4^- and $CH_3SO_3^-$) rather than previously proposed SO_4^{2-} significantly promotes the anisotropic nanowire growth of hexagonal WO_3.